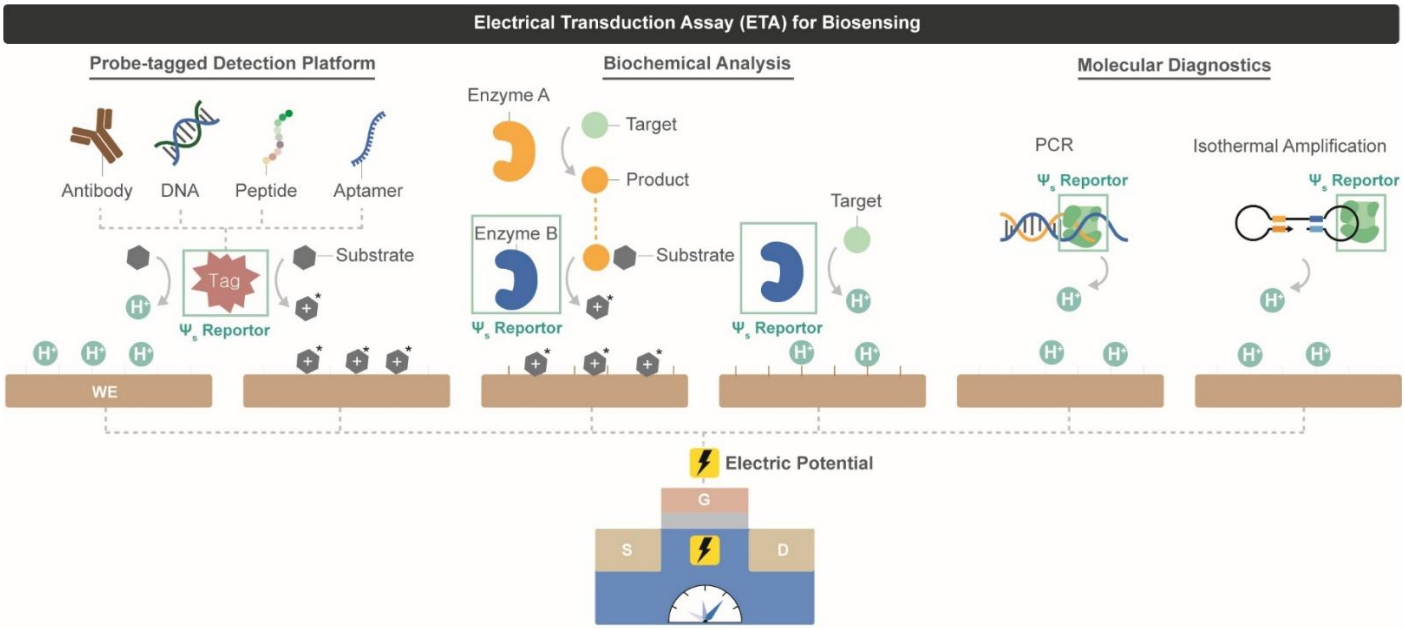

Extended Data Fig. 1 | related to Fig. 1: Ψ_s reporter concept and its application in ETA. The Ψ_s reporter is defined as any reaction element that converts a specific biological event into the generation of charged products that modulate the Ψ_s at the WE, which is connected to the FET gate. Here, G, S, and D denote the gate, source, and drain terminals, respectively. In probe-tagged detection formats, enzymes such as HRP are conjugated to recognition elements—including antibodies, nucleic acids, peptides, or aptamers—and function as Ψ_s reporters by generating protons and charged reaction intermediates during substrate turnover. In biochemical analysis, single-enzyme reactions or enzyme cascades produce charged substrates or protons that interact with the electrode interface and induce changes in Ψ_s. In molecular amplification processes, including polymerase chain reaction and isothermal amplification, nucleotide incorporation catalyzed by polymerases intrinsically releases protons and generates charged byproducts, including polynucleotides, pyrophosphate, orthophosphate, magnesium ions (Mg^{2+}), potassium ions (K^+), and ammonium ions (NH_4^+), positioning polymerase activity itself as a direct reporter for Ψ_s transduction. Debye length limitations observed in conventional FET biosensors can be overcome by detecting the generated charged products, which produce strong charge accumulation on the WE regardless of ionic strength. This mechanism is further discussed in the *Materials Screening for ETA control* section.

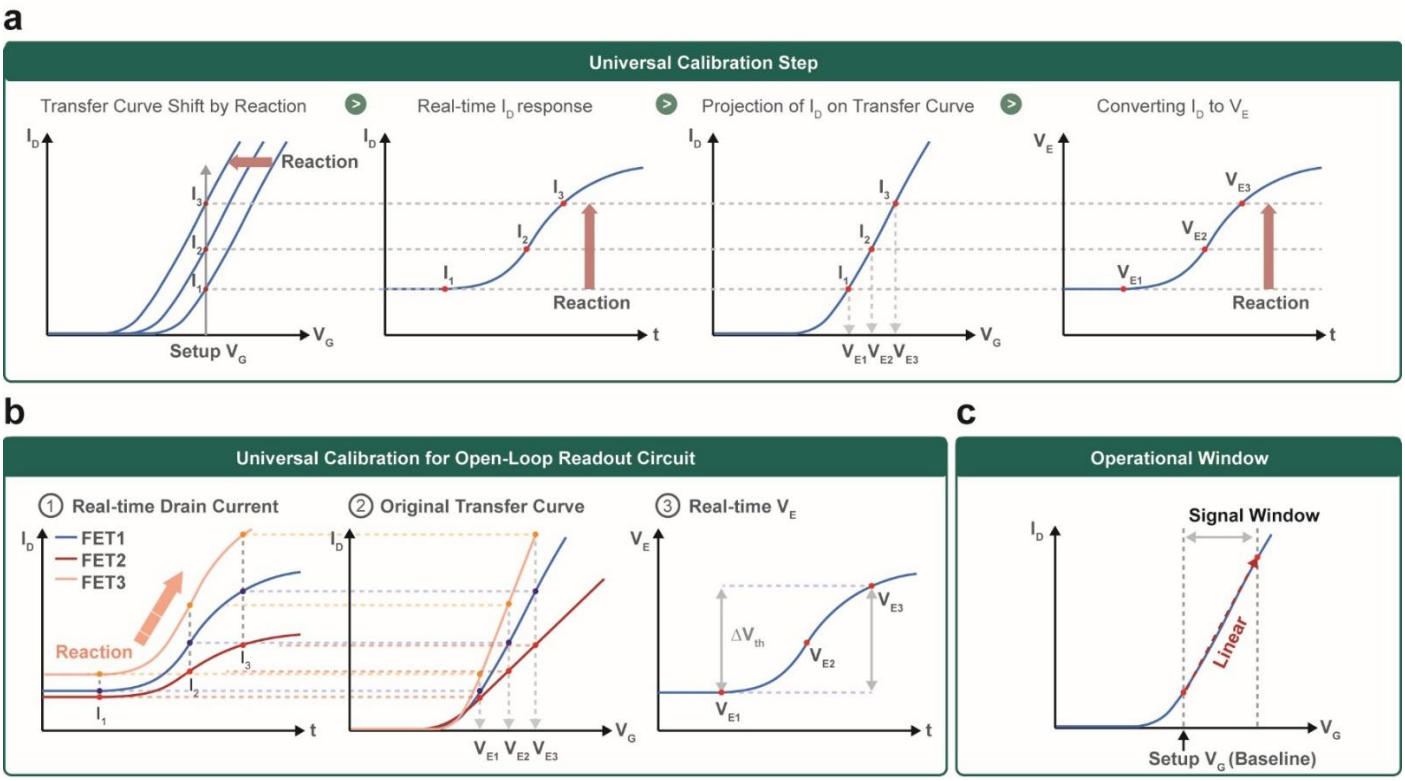

Extended Data Fig. 2 | related to Fig. 2: Universal calibration method for open-loop FET operation. (a) Schematic workflow of the universal calibration method. Biological events induce a parallel shift of the transfer curve, which produces changes in real-time I_D at fixed V_G and V_D. Each measured I_D value is projected onto the pre-stored original transfer curve to obtain the corresponding V_G (i.e. V_{E1}, V_{E2}, V_{E3}) converting real-time I_D responses into real-time V_E. (b) Example of the calibration effectiveness. Real-time I_D responses recorded from different FETs illustrate device-to-device variation arising from intrinsic differences in transfer curve characteristics. The pre-stored original transfer curves serve as the reference mapping function for calibration, allowing each measured current level to be converted to its corresponding V_G (i.e. V_{E1}, V_{E2}, V_{E3}). Through this current–voltage mapping, calibrated real-time V_E traces are obtained, enabling direct extraction of biological event-induced ΔV_{th} in terms of ΔV_E, which also corresponds to $\Delta \Psi_s$. (c) The operational window denotes the linear region of the transfer curve in which the calibrated output exhibits a linear response proportional to the reaction. The applied V_G is set within the linear region, which defines the baseline V_E in real-time V_E measurement.

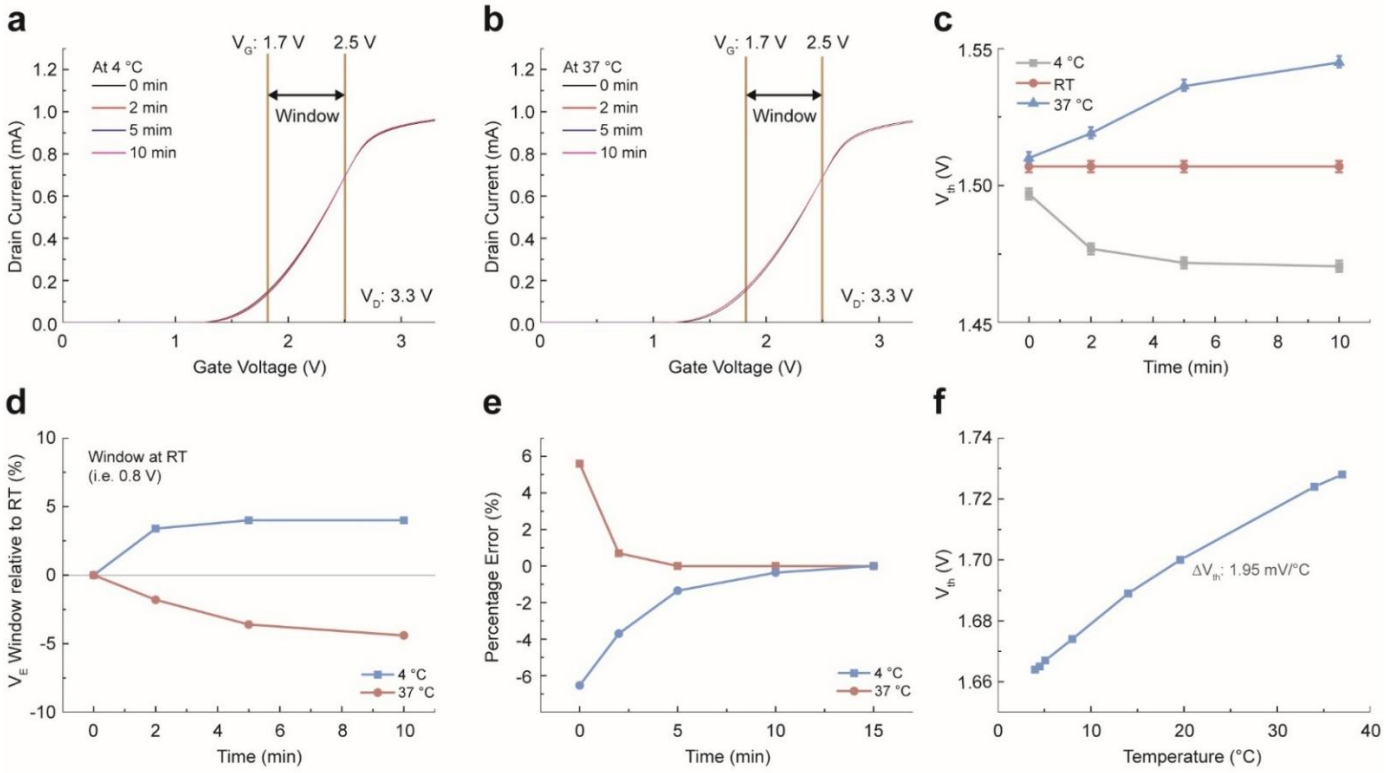

Extended Data Fig. 3 | related to Fig. 2: Temperature-dependence and equilibration behavior of the portable open-loop reader. (a) Transfer curves measured at 4 °C after 0, 2, 5, and 10 min. The V_G window was set to 1.7–2.5 V, corresponding to the linear region of the transfer curve used for routine operation, and shows a gradual rightward shift that relaxes toward a stable profile as the device equilibrates to the low-temperature environment. (b) Transfer curves measured at 37 °C under the same timing sequence, exhibiting an opposite left-shift relative to room temperature (RT) and similarly converging after ~5–10 min. (c) Extracted V_{th} over time at 4 °C, RT (20 °C), and 37 °C, demonstrating that temperature perturbations induce transient shifts of ~30–40 mV that decay toward steady-state values with a characteristic thermal equilibration period. (d) Bias percentage of V_E within the defined V_G window (1.7–2.5 V), referenced to the RT condition, showing temperature-induced changes in V_E at 4 °C and 37 °C. The V_E bias exhibits opposite-direction shifts at low and high temperatures and stabilizes within ~10 min, remaining within ±5% across 4–37 °C. (e) Percentage error of V_E as a function of equilibration time, calculated by normalizing the measured V_E at each time point to the corresponding fully equilibrated V_E value at each temperature (4 °C or 37 °C). The data show that the measurement error decreases with equilibration and returns to within ±2% after ~5 min. (f) Steady-state V_{th} as a function of temperature, revealing a near-linear dependence consistent with the temperature coefficient of silicon FET threshold voltage (~1.95 mV/°C). This V_E based temperature correction was applied in Figure 2c.

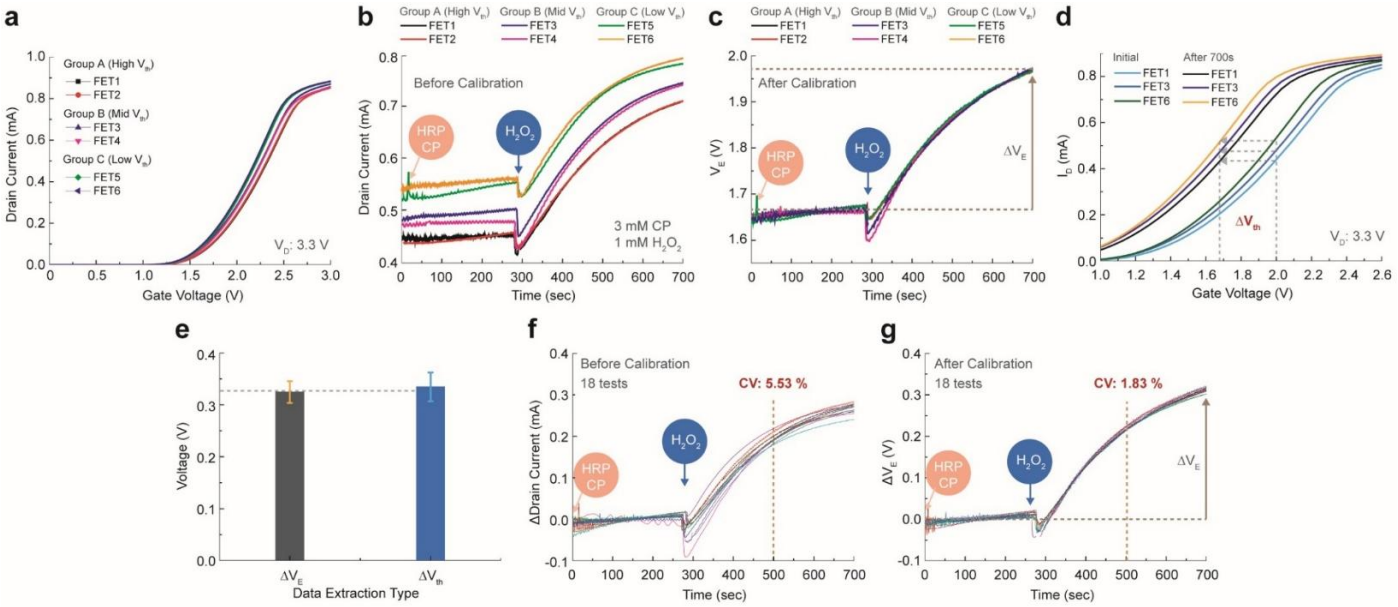

Extended Data Fig. 4 | related to Fig. 2: Calibration evidence. (a) Transfer curves of six commercial FETs grouped by high, mid, and low V_{th} at V_D = 3.3 V, illustrating intrinsic device-to-device electrical variability. (b) Real-time I_D responses from the same six FETs under identical HRP/CP/H_2O_2 conditions (8 ng/mL HRP, 1 mM H_2O_2, 3 mM CP), showing substantial variation in raw I_D signals due to differences in transfer curve shape. (c) Calibrated V_E traces derived from the responses in (b), demonstrating effective calibration across devices and confirming that the universal calibration strategy compensates for device-dependent electrical variability. (d) Transfer curves of three representative FETs (FET1, FET3, FET6) measured before and after 700 sec of HRP reaction, illustrating the HRP signal-induced ΔV_{th}. (e) Comparison of HRP-CP system-induced potential changes extracted using the calibrated ΔV_E from (c) versus the ΔV_{th} extracted from (d). The close agreement demonstrates that ΔV_E quantitatively reproduces ΔV_{th}. (f) Real-time I_D responses from 18 repeated tests measured under identical HRP/CP/H_2O_2 conditions, normalized to 0 mA before calibration. Substantial device-to-device variation is observed due to intrinsic differences in transfer curve characteristics, with a CV of ΔI_D of 5.53% at 500 sec. (g) Calibrated ΔV_E traces from the same 18 tests normalized at 0 V, obtained by converting real-time current signals into V_E shifts through the universal calibration process. Calibration markedly reduces device-dependent variation, yielding a CV of ΔV_E 1.83%.

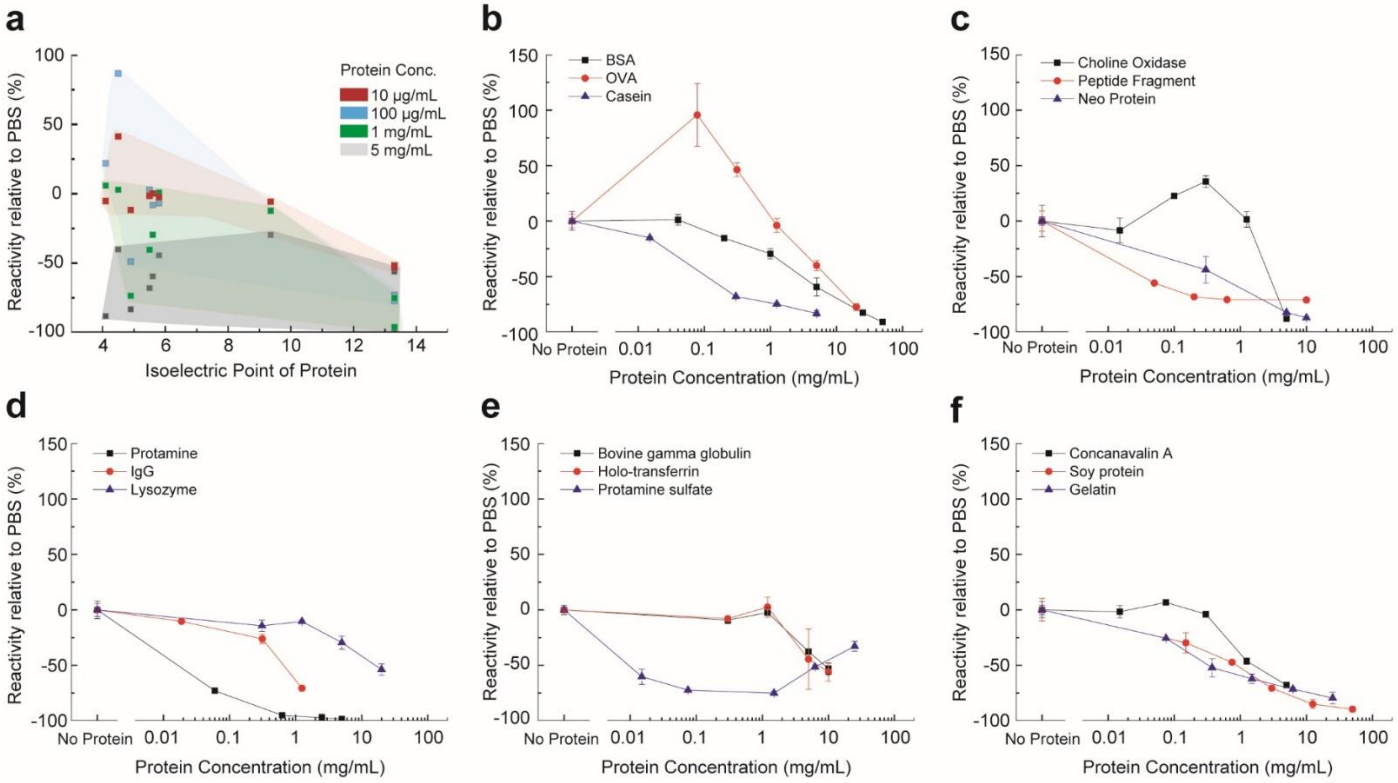

Extended Data Fig. 5 | related to Fig. 3: Protein pI–dependent modulation of reactivity in PBS. (a) Reactivity normalized to the no-protein PBS control plotted as a function of protein pI for four protein concentrations (10 µg/mL, 100 µg/mL, 1 mg/mL, and 5 mg/mL). At low protein concentrations (10–100 µg/mL), reactivity shows a clear pI-dependent trend, with lower-pI proteins producing weaker modulation and higher-pI proteins inducing stronger suppression. At higher concentrations (1–5 mg/mL), this pI dependence is lost, and HRP reactivity is uniformly suppressed across all proteins. Data in (a) are extracted from the concentration-dependent measurements shown in (b–f). Reactivity as a function of protein concentration is shown for (b) BSA, ovalbumin, and casein; (c) ChOx, peptide fragment, and Neo protein; (d) protamine, IgG, and lysozyme; (e) bovine gamma globulin, holo-transferrin, and protamine sulfate; and (f) concanavalin A, soy protein, and gelatin.

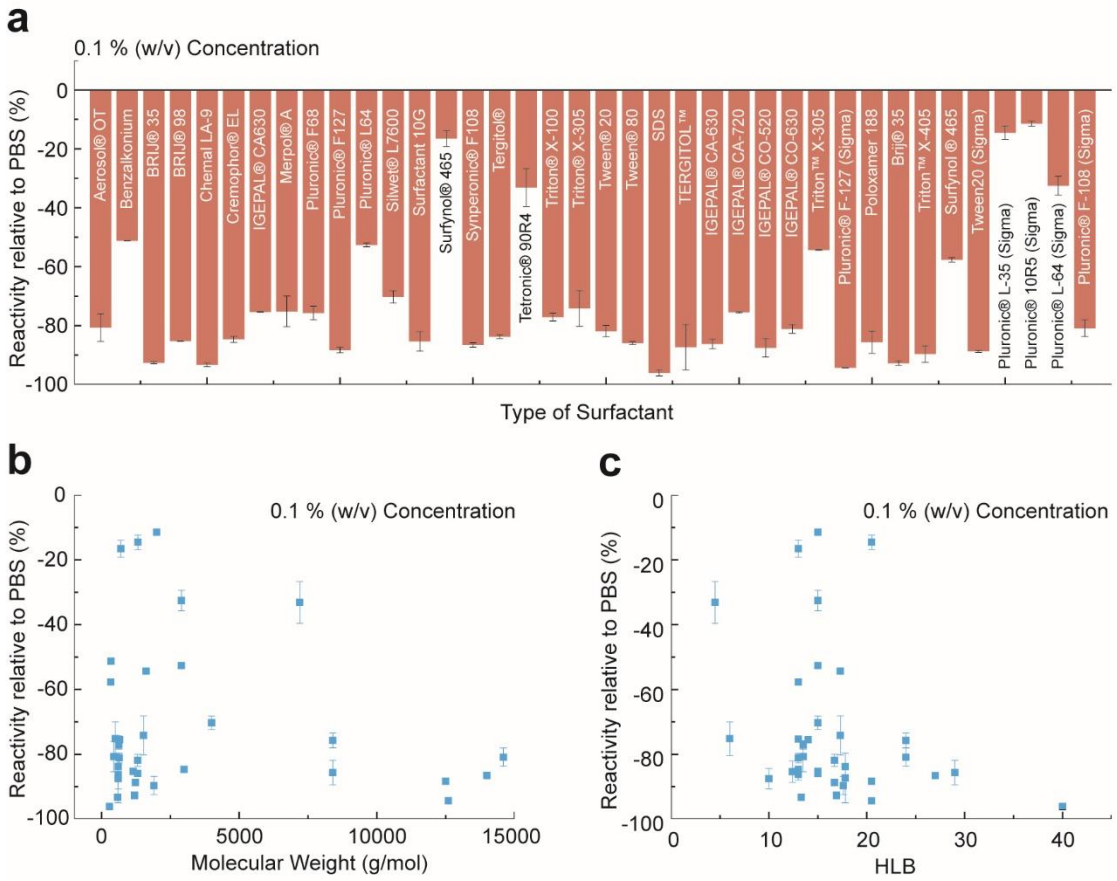

Extended Data Fig. 6 | related to Fig. 3: Surfactant screening for solution-state measurement. (a) Reactivity relative to the no-surfactant PBS control measured in the presence of 38 different surfactants at 0.1% (w/v), spanning ionic, nonionic, and zwitterionic species, showing broad surfactant-dependent modulation of HRP signal responses. (b) Reactivity relative to the no-surfactant PBS control plotted as a function of surfactant MW of tested surfactants, indicating that higher–MW surfactants generally induce stronger suppression, while lower–molecular-weight surfactants tend to have a reduced impact. (c) Reactivity relative to the no-surfactant PBS control plotted as a function of HLB of tested surfactants, showing no clear monotonic trend overall, although surfactants with intermediate HLB values (~14–18) exhibit relatively minimal impact, whereas high-HLB surfactants tend to produce stronger suppression.

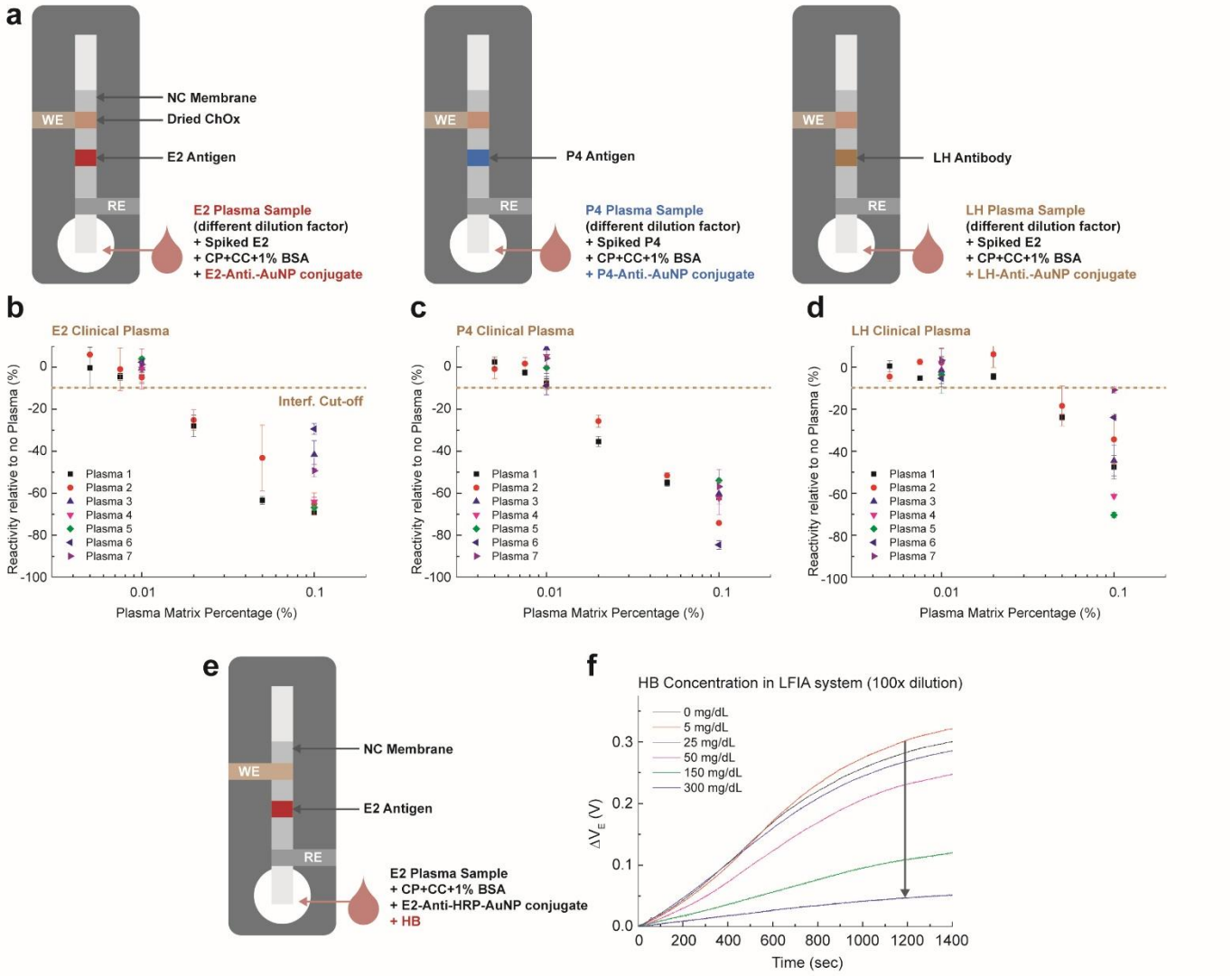

Extended Data Fig. 7 | related to Fig. 4: Effects of dilution and HB interference on reactivity in solid-state measurement. (a) Experimental condition for evaluating plasma matrix effects in LFIA system for E2, P4, and LH using clinical plasma samples at different dilution factors, with 1% BSA, CP/CC, and the corresponding 50 mOD antibody–AuNP–HRP conjugates. To maintain identical antigen input across all conditions, target antigens were spiked such that the total antigen amount remained constant across dilution ratios. Reactivity measured for (b) E2, (c) P4, and (d) LH across seven clinical plasma samples as a function of plasma matrix percentage, normalized to the no-plasma 1% BSA condition. At 100× dilution, responses remain above the predefined interference cutoff (−10%), indicating negligible plasma matrix interference under the measurement setup, whereas higher plasma fractions induce pronounced signal suppression. (e) Experimental conditions used to evaluate HB interference. E2 clinical plasma samples and HB were diluted 100× in the running buffer including CP/CC, 1% BSA, and 50 mOD E2–antibody–HRP–AuNP conjugates. Accordingly, the actual (pre-dilution) HB concentrations evaluated in this study correspond to 0, 0.5, 2.5, 5, 15, and 30 g/dL. (f) Representative real-time V_E traces measured at increasing HB concentrations in the LFIA system under 100× dilution conditions. Initial baseline V_E trace was subtracted to highlight the reaction kinetics only. At HB levels corresponding to the clinical evaluation range used in this study (≤25 mg/dL), electrical response remains comparable to the HB-free condition, indicating negligible hemoglobin-induced interference. Noticeable signal suppression is observed only at excessively high HB concentrations, well beyond the measurement conditions relevant to practical assay condition.

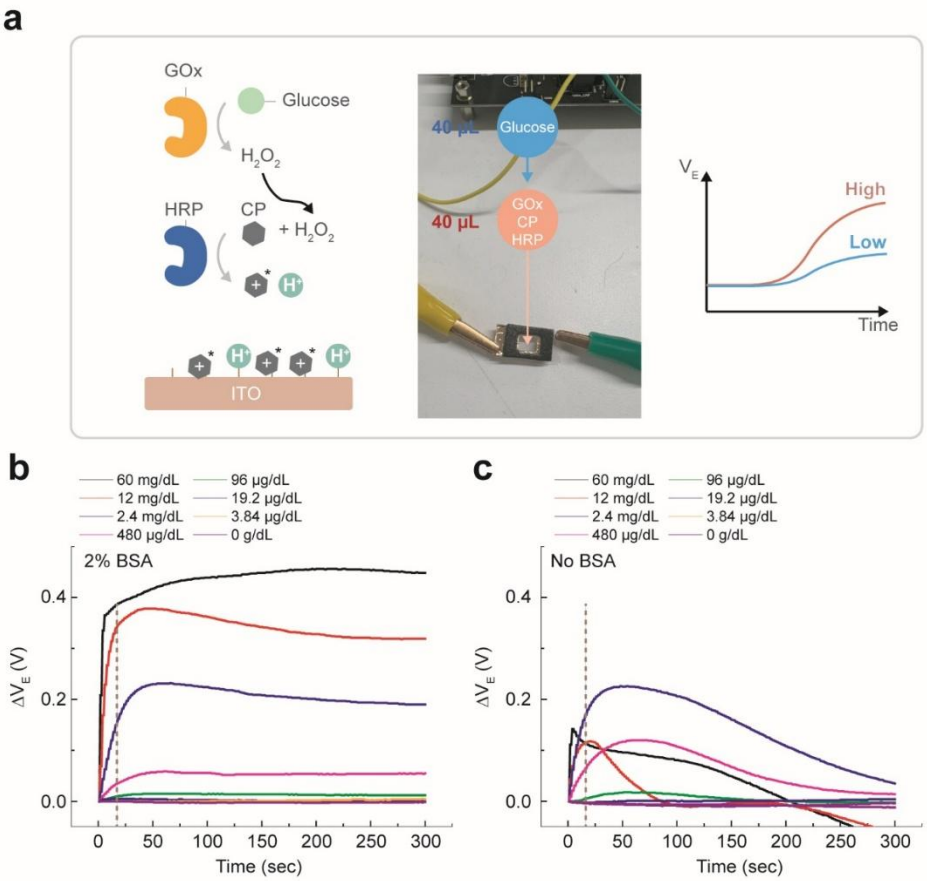

Extended Data Fig. 8 | related to Fig. 4: Glucose detection using solution-state measurement. (a) Schematic of glucose sensing and experimental setup. Glucose is oxidized by GOx to generate H_2O_2, which subsequently drives the HRP–CP reaction to produce protons and charged substrates at the ITO interface. The right panel shows the measurement configuration, where GOx/CP/HRP solution and glucose are sequentially introduced (40 µL each) onto the well-type electrode. (b) Representative real-time ΔV_E responses measured in the presence of 2% BSA for glucose concentrations ranging from 0 to 60 mg/dL. Increasing glucose levels produces larger V_E shifts. (c) Real-time ΔV_E responses measured without BSA, showing reduced stability and distorted concentration dependence due to excessive surface reactivity and interference, which disrupts normal signal progression. Excessively high GOx activity can adversely affect system stability and compress the dynamic range of the electrical readout. This effect can be mitigated by adding appropriate base proteins such as BSA, which suppress excessive HRP reactivity and thereby expand the usable dynamic range.

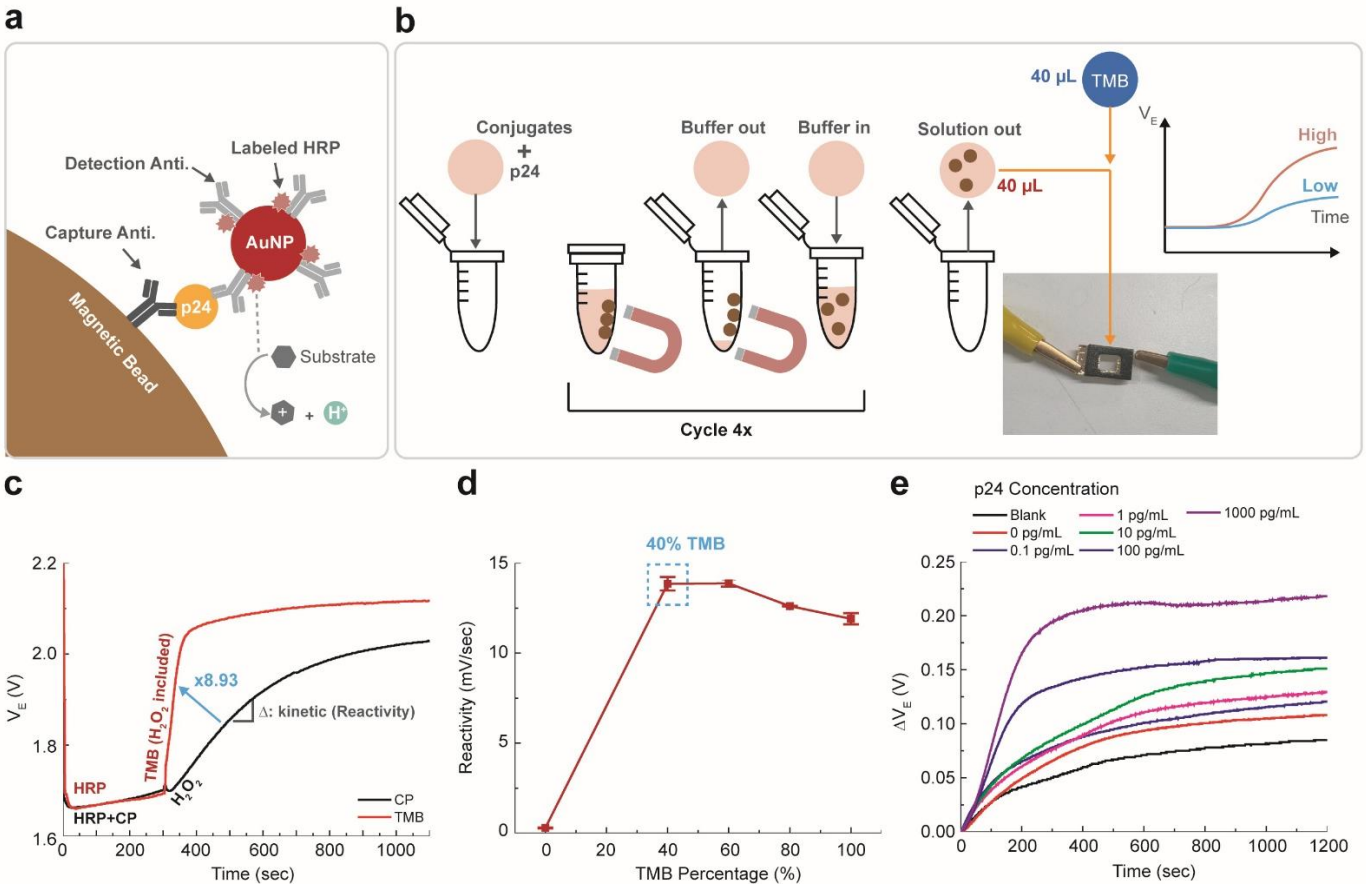

Extended Data Fig. 9 | related to Fig. 4: Electrical readout of IMS system. (a) Schematic of the IMS assay design. Target p24 is captured by capture antibodies immobilized on magnetic beads and subsequently labeled with HRP–AuNP conjugates via detection antibodies, forming a bead–p24–HRP–AuNP complex. Upon substrate addition, HRP catalysis generates protons and charged substrates that are transduced into an electrical signal. (b) IMS workflow and electrical readout. Samples containing p24 are incubated with capture antibody-functionalized magnetic beads and detection antibody–HRP–AuNP conjugates, followed by magnetic separation and repeated buffer exchange (4×) to remove unbound species. The final bead suspension is introduced into the well-type electrode, where TMB/ H_2O_2 solution separately added to initiate HRP catalysis, producing a concentration-dependent V_E response that enables quantitative detection. (c) Representative real-time V_E traces comparing CP and TMB substrates measured under identical HRP conditions (20 ng/mL HRP), where CP was tested with 3 mM CP and 1 mM H_2O_2, and TMB was tested using a commercial ELISA-grade TMB solution containing H_2O_2, showing a markedly enhanced interfacial response with TMB. The kinetic reactivity (ΔV_E/sec) obtained with TMB is increased by approximately 8.93-fold relative to CP, indicating substantially faster charge-generation dynamics. (d) Reactivity as a function of TMB percentage in the substrate mixture measured at 20 ng/mL HRP, identifying an optimal composition around 40% TMB that maximizes ETA response before signal saturation or decline at higher TMB fractions. Despite its high reactivity, TMB exhibits limited solution stability, restricting its practical use to controlled laboratory settings rather than long-term or field-deployable assays[29]. (e) Representative ΔV_E traces normalized to 0 V for increasing concentrations of HIV p24 following immunomagnetic separation. The blank condition contains magnetic beads only, without antibody–antigen conjugates, and reflects baseline drift and nonspecific signals arising from the TMB–H_2O_2 reaction. The ΔV_E signals were quantified at 20 min, with the blank signal subtracted to obtain concentration-dependent responses across the tested range (0.1–1000 pg/mL).

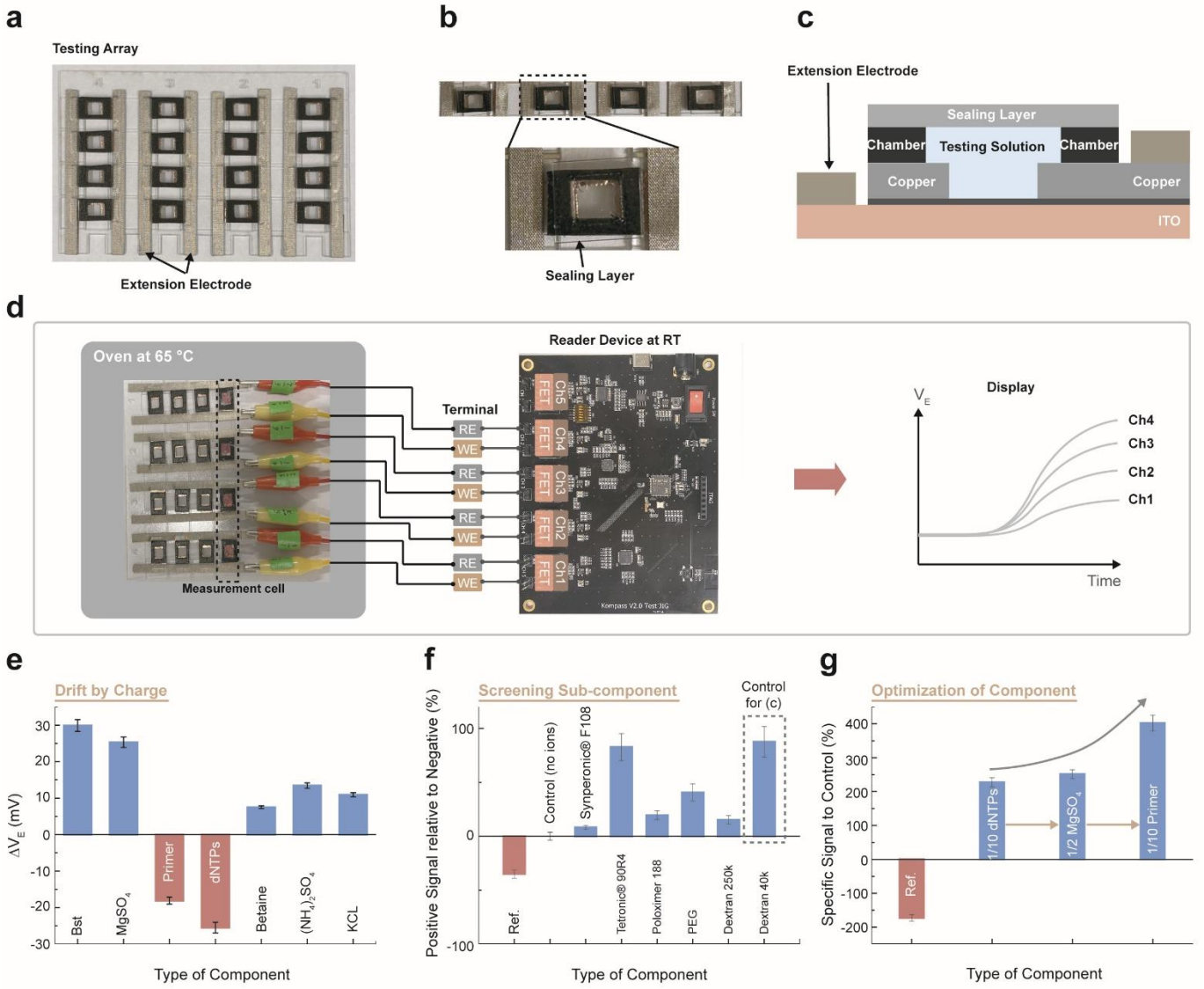

Extended Data Fig. 10 | related to Fig. 4: Solid-state measurement for LAMP system and stepwise optimization of LAMP components. (a) Photograph of the well-type electrode array designed for multiplexed LAMP, comprising multiple measurement cells with integrated extension electrodes for parallel electrical interfacing. (b) Photograph of the sealed reaction chambers. The sealing layer prevents evaporation and drying of the LAMP reaction solution during isothermal amplification at 65 °C, ensuring stable reaction conditions throughout the assay. (c) Cross-sectional schematic of a single well-type electrode cell, illustrating the ITO WE, copper RE, extension electrode, sealed chamber, and confined LAMP reaction solution. (d) Parallel LAMP measurement setup. Multiple sealed well-type electrodes are incubated in an oven for isothermal amplification and subsequently connected to a multichannel reader device at room temperature for simultaneous real-time V_E acquisition (Ch1–Ch4), demonstrating scalable and multiplexed electrical readout for LAMP. (e) ΔV_E shifts measured at 65 °C over 300 sec are induced by individual LAMP reaction components, all of which can influence LAMP kinetics and the electrical readout. Measurements were performed in a Tris–HCl base buffer (pH 8.8) containing each component under otherwise identical conditions. Strongly charged species, particularly primers and dNTPs, generate pronounced negative potential shifts and act as signal-suppressing components, whereas salts and stabilizing additives (e.g., $MgSO_4$, $(NH_4)_2SO_4$, and KCl as ionic components, and betaine as an additive for amplification enhancement induce positive shifts of varying magnitude, highlighting their direct impact on the electrical signal during LAMP. (f) Screening of LAMP

sub-components and additives for optimization of the LAMP system for electrical readout, shown as signal relative to the negative control condition without heating, with the signal defined as ΔV_E measured at 300 sec. All measurements were performed in a Tris–HCl base buffer (pH 8.8), with betaine, $(NH_4)_2SO_4$, and KCl excluded from the conventional fluorescence-optimized reference mixture (Supplementary Fig. 25) to eliminate baseline drift originating from individual components observed in panel (e). Signal values represent the difference between the negative condition (no heating) and the positive condition (65 °C) after 1 h incubation, with 0.5% (w/v) of each additive individually introduced. Among the tested additives, dextran markedly enhances the ETA signal while maintaining signal stability, identifying it as a favorable component for LAMP optimization for electrical readout. (g) Stepwise optimization of selected components based on panel (f), demonstrating monotonic enhancement of the specific electrical signal through systematic adjustment of dNTPs, $MgSO_4$, and primer concentrations. The specific signal is defined as the difference in ΔV_E measured at 300 sec between the positive (heated) and negative (no-heating) samples, normalized to the control condition defined in panel (f). The control condition corresponds to the simplified baseline composition consisting of Tris–HCl buffer (pH 8.8) supplemented with dextran at 0.5% (w/v) and excluding fluorescence-optimized components. The optimized composition yields a several-fold signal increase relative to this baseline condition, establishing reaction conditions suitable for robust electrical readout of LAMP.